Optics Communications 514 (2022) 128163

Contents lists available at ScienceDirect

Optics Communications

journal homepage: www.elsevier.com/locate/optcom

Space-based correction method for LED array misalignment in Fourier ptychographic microscopy

Youqiang Zhu [a], Minglu Sun [a,b], Peilin Wu [a,b], Quanquan Mu [a,b], Li Xuan [a,b], Dayu Li [a,*], Bin Wang [a,b,*]

[a] Changchun Institute of Optics, Fine Mechanics and Physics, Chinese Academy of Sciences, Changchun 130033, China
[b] Center of Materials Science and Optoelectronics Engineering, University of Chinese Academy of Sciences, Beijing 100049, China

ARTICLE INFO

Keywords:
Computational imaging
Fourier ptychographic microscopy
Misalignment
Particle swarm optimization

ABSTRACT

Fourier ptychographic microscopy is a super-resolution technique, which could break through the Space-Band-Product (SBP) limit of the system by employing varied-illumination and phase retrieval algorithm. A LED array is used to provide angularly varying illuminations, which is portable and cheap. However, the installation accuracy of the LED array is not sufficient, resulting in position misalignment errors. The misalignment errors not only cause the calculation error of the sub-apertures in the frequency domain, but also the artifacts in reconstruction images. Although some correction methods have been proposed, the correction ability of these methods cannot deal with the misalignment errors well. In this paper, we proposed a misalignment errors correction method. This method uses the Particle swarm optimization (PSO) algorithm to search the four misalignment parameters (Δx, Δy, θ, Δh) in space domain. It is termed as Space based correction (SBC) method. Compared with the state-of-art methods, the SBC method is more stable and accuracy.

1. Introduction

Fourier ptychographic microscopy is a recently developed computational imaging technology, which possesses the advantages of wide field-of view (FOV) and high-resolution [1,2]. Like the conventional ptychography [3–5], FPM shares its roots with synthetic aperture [6–8] and phase retrieval [9–13].

In a typical FPM system, a LED array light source is used to provide angle-varied illumination. Based on the angle-varied illumination, the information exceeding the diffraction limit of the system can be transferred into the objective lens. After turning on the LED light source sequentially, a series of low-resolution images have been recorded. Then an iteratively multi-image-fusion process in frequency domain is implemented. The final NA of the system is equal to the sum of the objective$_{NA}$ and the illumination$_{NA}$. In order to solve the problems existed in the original FPM, many studies have been reported. Aiming to improve the signal-to-noise of the dark-field images and illumination$_{NA}$, some system improvement schemes like condenser [14], dome LED model [15,16] and hemisphere LED model [17] have been proposed. To reduce the acquisition time, a series of methods like multi-coding illumination [18–20], single shot [21–24] have been reported. In addition, there are also some methods focusing on the aberration correction [25–28], noise suppress [29–32] and vignetting effect removing [33].

FPM faces a serious problem that is the misalignment errors. Due to the limited installation accuracy of LED array, its actual position will be different from the ideal position, and the reconstruction quality will have a degradation. In order to solve this problem, several correction methods have been proposed. Firstly, the searching process is implemented in frequency domain. Most of the correction methods in the frequency domain are based on simulated annealing(SA) algorithm [34,35]. During the searching process, every LED has a specific sub-aperture position, and every sub-aperture has been searched until the cost function value is minimum. Its search time is long and more likely to fall into local minimum, because of the large number of sub-apertures. Different from the conventional SA algorithm that searching all the sub-apertures in frequency domain, Sun et al. proposed a positioning correction approach, named pcFPM. The method combines the SA algorithm and non-linear regression technique [36]. The method not only gives a better initial value by correcting the bright-field images, but also improves the iterating efficiency and adjusting accuracy by introducing a global positional misalignment model of the LED array. However, due to the limited search time, at the same time, the high-resolution spectrum does not initialize during the last iteration. As a result, the performance of the pcFPM is limited. Secondly, the searching process is implemented in space domain [37,38]. Based on the searching process implemented in space domain, Zhou et al. proposed a mcfpm method by using the SA algorithm [37]. The method searches

* Corresponding authors.
E-mail addresses: lidayu@ciomp.ac.cn (D. Li), 175969722@qq.com (B. Wang).

https://doi.org/10.1016/j.optcom.2022.128163
Received 18 January 2022; Received in revised form 1 March 2022; Accepted 6 March 2022
Available online 14 March 2022

the shift parameters (Δx, Δy) and rotation parameter (θ) in space domain, but it does not correct the height (h) parameter. At the same time, the global converge accuracy of the SA algorithm is not sufficient when there are lots of parameters.

In this paper, a Space based Correction (SBC) method is proposed for misalignment errors. Different from the above methods, SBC uses the particle swarm optimization (PSO) algorithm to correct the four position error parameters (Δx, Δy, θ, Δh) in the space domain directly. Compared with the SA algorithm, PSO has better global convergence. Compared with the traditional methods, the searching accuracy is improved and the final reconstruction results are artifacts free. Both in the simulations and the experiments, the results of SBC are better than the state-of-art algorithms. Section 2 introduces the principle of the SBC. Section 3 and Section 4 illustrate the performance of SBC in simulations and experiments, respectively. At last, conclusion is surmised in Section 5.

2. Principle

2.1. Misalignment model of FPM

A typical FPM system consists of five parts: a LED array, a low-NA objective lens, a tube lens and a detector, shown in Fig. 1. When the LEDs are turning on sequentially, the sample is illuminated by spherical wave with different angles. The whole sample will be divided into pieces to accomplish a plane wave approximate. Then the information exceeds the diffraction limit can be shifted into the objective and received by the detector. Each LED has its own illumination angle, which corresponds to the specific position of the sub-aperture in the frequency domain. Therefore, it is necessary that the known spatial position of the LED array is correct. In practice, it is inevitable that there will be misalignment errors in the FPM system. These misalignment errors will lead to the quality degradation of the reconstructed high-resolution images. Before finding the misalignment errors, a misalignment model should be established. When the ith LED (m row, n col) is turned on, the wavevector of one sub-field can be expressed as

$$(k_x^i, k_y^i) = \frac{2\pi}{\lambda}\left(\frac{x_c - x_i}{\sqrt{(x_c - x_i)^2 + (y_c - y_i)^2 + h_0{}^2}}, \frac{y_c - y_i}{\sqrt{(x_c - x_i)^2 + (y_c - y_i)^2 + h_0^2}}\right) \tag{1}$$

where (x_c, y_c) is the center of the sub-field, (x_i,y_i) is the position of ith LED, h_0 is the distance between the LED array and the sample. The misalignment errors include shift (Δx, Δy), rotation (θ) and height error Δh, and the misalignment model is shown in Fig. 2. Then, the position of each LED with misalignment errors can be expressed as

$$\begin{aligned} x^i{}_{m.n} &= d_{LED}[\cos(\theta)m + \sin(\theta)n] + \Delta x \\ y^i{}_{m.n} &= d_{LED}[-\sin(\theta)m + \cos(\theta)n] + \Delta y \end{aligned} \tag{2}$$

where d_{LED} denotes the distance between the adjacent LED elements. After being affected by the misalignment errors, the wavevectors can be rewritten as

$$(\mu^i, \nu^i) = \frac{2\pi}{\lambda}\left(\frac{x_c - x_i}{\sqrt{(x_c - x_i)^2 + (y_c - y_i)^2 + (h_0 + \Delta h)^2}}, \frac{y_c - y_i}{\sqrt{(x_c - x_i)^2 + (y_c - y_i)^2 + (h_0 + \Delta h)^2}}\right) \tag{3}$$

2.2. Space-based correction algorithm

Similar to the correction method [37] implemented in the spatial domain, we propose an iterative correction method based on the particle swarm optimization (PSO) algorithm, which is called space-based correction (SBC) method. Fig. 3 shows the flow chart of SBC. SBC includes searching process and reconstruction process. During the searching process, different from the mentioned method, we correct the misalignment errors for four dimensions instead of three. The connection between particles ensures that the global convergence of PSO algorithm is better than that of SA algorithm.

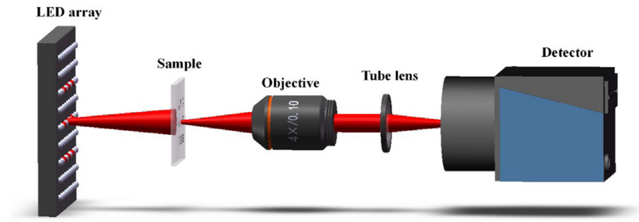

Fig. 1. The typical FPM system.

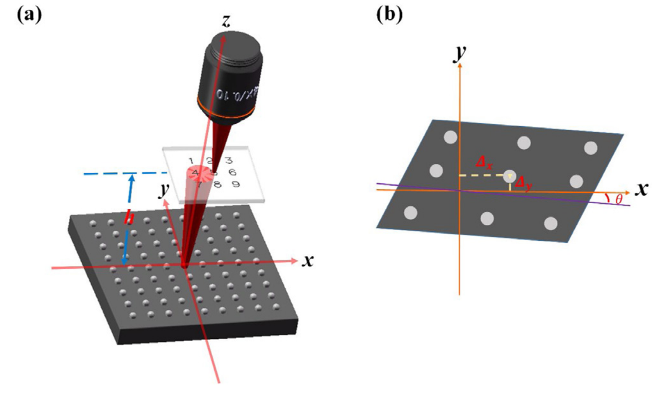

Fig. 2. The FPM system with misalignment errors.

We introduce the reconstruction process of SBC first. At the beginning, it is necessary to remove the low-resolution images that affected by vignetting effect. Once these images are involved in the reconstruction process, the reconstructed high-resolution spectrum will fall into the local minimum value, [33], and so will the correction process. We choose to use the threshold method to find the low-resolution images affected by the vignetting effect, and then abandon them during the reconstruction process [33]. In order to adapt most of the samples and microscopy, the threshold we used is 0.1∼0.8. Secondly, a high-resolution object estimates $O_0(\mu, \nu)$ and pupil fiction $P_0(\mu, \nu)$ are initialized. Thirdly, generate a low-resolution image estimate in frequency domain, which corresponding to the ith LED with the wavevector (μ^i, ν^i), and can be expressed as

$$\varphi^i_{m,n}(x, y) = \mathcal{F}^{-1}\{O_0(\mu - \mu^i, \nu - \nu^i) * P_0(\mu, \nu)\} \tag{4}$$

Fourthly, impose the intensity constraint with the captured images by

$$\phi^i_{m,n}(x, y) = \sqrt{I^{m,n}_{capture}(x, y)}\frac{\varphi^i_{m,n}(x, y)}{\left|\varphi^i_{m,n}(x, y)\right|} \tag{5}$$

where $\phi^i_{m,n}(x, y)$ and $\varphi^i_{m,n}(x, y)$ are the complex low-resolution images with and without intensity replacement respectively. Then, an updated Fourier transform of low-resolution image is calculated by $\Phi^i_{m,n}(\mu, \nu) = \mathcal{F}\{\phi^i_{m,n}(x, y)\}$. Fifthly, updating the object and the pupil function with the EPRY [25] algorithm:

$$\begin{aligned} O_{i+1}(u - u_{m,n}, v - v_{m,n}) &= O_i(u - u_{m,n}, v - v_{m,n}) + \frac{P(u,v)^*}{|P(u,v)|^2_{\max}}\Phi' \\ P_{i+1}(u, v) &= P_i(u, v) + \frac{O_i(u-u_{m,n},v-v_{m,n})^*}{|O_i(u-u_{m,n},v-v_{m,n})|^2_{\max}}\Phi' \end{aligned} \tag{6}$$

where Φ' is defined as

$$\Phi' = \Phi(\mu + \mu^i_{m,n}, \nu + \nu^i_{m,n}) - O_i(\mu + \mu^i_{m,n}, \nu + \nu^i_{m,n}) * P_0(\mu, \nu) \tag{7}$$

Sixthly, repeat the 3–5 until all the images have been updated. Seventhly, repeating the 3–6 J times, and J will be defined in search phase.

As mentioned above, the search algorithm SBC used is PSO algorithm. In the PSO algorithm, K particles are generated and every particle has four misalignment parameters (Δx, Δy, θ, Δh). The cost function in SBC is defined as

$$E = \frac{1}{x * y} \min_{\Delta x,\Delta y,\theta,\Delta h} \sum_{m,n} \sum_{x,y} \left| I^{m,n}_{captured} - I^{m,n}_{SBC}(p_{\Delta x,\Delta y,\theta,\Delta h}) \right|^2 \tag{8}$$

where $I^{m,n}_{SBC}(p_{(\Delta_x,\Delta_y,\theta,\Delta_h)})$ is the corresponding intensity image estimate using conventional FPM (step 2–7) with a misalignment error (Δx, Δy, θ, Δh), and $p_{(\Delta_x,\Delta_y,\theta,\Delta_h)}$ denotes the particle with misalignment error (Δx, Δy, θ, Δh) in PSO. PSO algorithm through the connection between the particles and the iteration process to find the global minimum value. Note that the captured images affected by the vignetting effect is also neglected in the cost function calculated process. The procedure of FPM reconstruction process in searching process of SBC only iterates 2 times. Too many iterations for reconstruction process will lead to unnecessary time consumption, and 2 iterations are sufficient in SBC. Next, we introduce the searching process of SBC.

The search process of SBC is divided into initialization process, rough search and precise search. Similar to other search algorithms, a good initial solution is important for SBC. It is difficult to give an initial solution with four parameters (Δx, Δy, θ, Δh), so we choose to find the initial solution in shift parameters (Δx, Δy) first, and a similar strategy has been used by Zhang et al. [39]. The number of LED used in this reconstruction process is $S = 25$. During the initial searching process, $K = 50$ particles are generated randomly in $\Delta x \in$ [−1000 μm,1000 μm] and $\Delta y \in$ [−1000 μm, 1000 μm]. Then cost function value of all the particles are calculated to get the minimum cost function value and the corresponding particle [x_b, y_b,0, 0]. Next, a rough search process is implemented. $K = 30$ particles are generated randomly in $\Delta x \in [x_b - 250$ μm, $x_b + 250$ μm], $\Delta y \in [y_b - 250$ μm, $y_b + 250$ μm], $\theta \in [-5°, 5°]$ and $\Delta h \in$ [−1000 μm, 1000 μm]. Before the iteration, the best particle is set by $p_{best} =$ [x_b, y_b,0, 0] and the minimum cost function is set as Ep_{best}. In the whole iteration process, if the cost function value E_k of a particle p_k is less than the cost function value E_{best} of the best particle p_{best}, it will be regarded as the new best particle. At the first iteration $l = 1$, the position parameters of particles will not be updated. Once the iteration time l >1, the position parameters of particles are updated by:

$$\begin{aligned} &v_{k,j}(l+1) = phi * \{v_{k,j}(l) + c_1 r_1 [p_{k,j} - x_{k,j}(l)] + c_2 r_2 [p_{best,j} - x_{k,j}(l)]\} \\ &x_{k,j}(l+1) = x_{k,j}(l) + v_{k,j}(l), j = 1, 2 \ldots, 4 \end{aligned} \tag{9}$$

where j is the number of position parameters, $x_{k,j}$ is the position of the k_{th} particle, $v_{k,j}$ is the update step-size of the k_{th} particle, r_1 and r_2 are numbers generated randomly in [0∼1] to ensure the random motion. c_1 and c_2 are the learning factors which decide the particles how to running to the best particle p_{best}, phi is the compressibility factor to control the step-size $v_{k,j}$, which determined by c_1 and c_2

$$phi = \frac{2}{\sqrt{2 - (c_1 + c_2) - \sqrt{(c_1 + c_2)^2 - 4(c_1 + c_2)}}}. \tag{10}$$

When the iteration l >15, the searching process becomes an accurate searching process. The number of LED used in reconstruction process is changed into S = 121, and a natural selection process is added to the iterative process. Natural selection only ensures the best half of the particles to survive to the next iteration. The position and step size of the bad half will be replaced by that of the good half. At the end of the iteration, the best particle position is used to reconstruct the high-resolution complex images and the iteration time of this reconstruction is $J = 10$.

3. Simulations

We verify the validity of the SBC by simulation first. The system parameters used in simulation is shown in Table 1. The position errors are introduced in the system, with Δx of 1 mm, Δy of 1 mm, θ of 5 degrees and Δh of 1 mm. Two images are used in the simulation as the amplitude and phase images in our work. Both of them contain 512 × 512 pixels and have been normalized to [0,1]. A set of 225 low-resolution images with 128 × 128 pixels are generated by traditional FPM with position errors. Two state-of-art correction algorithm pcFPM and SA algorithm are used for comparison. Because the mcFPM only corrects the shift error (Δx, Δy) and rotation error (θ), and the actual misalignment errors are (Δx, Δy, θ, Δh), the SA algorithm is used to search the four misalignment errors to replace the mcFPM for comparison. In addition, a new evaluation criterion is used, which is calculated by the sum of pixel number difference between the corrected positions and the real positions of all sub-apertures in the frequency domain, noted as Δp. Fig. 4(a1) and Fig. 4 (b1) are the ground-truths. The reconstruction results of different algorithm are shown in Fig. 4(a2)–(a5) and Fig. 4 (b2)–(b5). Conventional FPM does not correct the misalignment errors, its reconstruction results are worse than the ground-truths, as shown in Fig. 4 (a2)–(b2). For the results of pcFPM, shown in Fig. 4(a3) and Fig. 4(b3), there are still some artifacts in the amplitude and phase images. The reason is once the iteration of it exceeds 8 times, its spectrum does not be initialized. At the same time, the position errors have not been corrected completely. The correction results of SA are shown in Fig. 4(a4) and Fig. 4(b4). Limited by the searching ability of SA algorithm, the reconstruction quality of the high-resolution amplitude and phase images are far from the ground-truths. The correction results of SBC are shown in Fig. 4(a5) and Fig. 4(b5). Benefiting from the strong search ability of PSO algorithm and the initialization strategy, the reconstruction amplitude and phase images are close to the ground-truth. The corrected misalignment errors are shown in Table 2, which shows the accuracy of the SBC is better than the other methods. In Fig. 5, red circles and black dots denote the corrected positions and the actual positions. It can be seen that almost all of the corrected positions of SBC have been located at the center of the red circles. Due to the large number of particles, the time of reconstruction process of SBC is ∼56s. For the pcFPM, expect for the non-linear regress process, the time of reconstruction process is ∼5s. For the SA, the time of reconstruction process is ∼55s. All algorithms are implemented in a Desktop computer (Intel Core i7-11700F,2.5 GHz). Most of time cost of SBC is the accurate search process. Fortunately, this method could correct the misalignment errors of the LED array. The misalignment parameters can be used to re-install optical system or reconstruct another imaging target with the corrected wavevector.

Table 1
Main parameters of the FPM system in simulation.

Incident wavelength	620 nm
Magnification of the objective	4×
NA of the objective	0.1
Pixel size of the detector	9 μm
Light source	A 15 × 15 LED array
Distance between the adjacent LEDs	4 mm
Distance between the sample and the LED array	66 mm

Table 2
Corrected results of different algorithm.

Algorithm	Δx/μm	Δy/μm	θ/°	Δh/μm	Δp	MSE
Convention FPM	0	0	0	0	4319	0.105
pcFPM	993.2	966.4	4.9754	1177.7	265	8×10^{-4}
SA	815.4	1069.9	3.1322	1099.4	1445	0.0049
SBC	1002.0	1000.3	5.0039	998.5	4	1.4×10^{-5}

In order to verify the stableness of the SBC, 50 simulations with random misalignment errors are performed. The position errors are generated randomly in $\Delta x \in$ [−1000 μm, 1000 μm], $\Delta y \in$ [−1000 μm, 1000 μm], $\theta \in [-5°, 5°]$ and $\Delta h \in$ [−1000 μm, 1000 μm]. Table 3 shows the mean square error (MSE) and Δp corrected by different algorithms. It is shown that the misalignment errors are almost corrected completely by SBC. For the average Δp in 50 simulations, it is only 9.3 pixel. The MSE of SBC is also smaller than other methods.

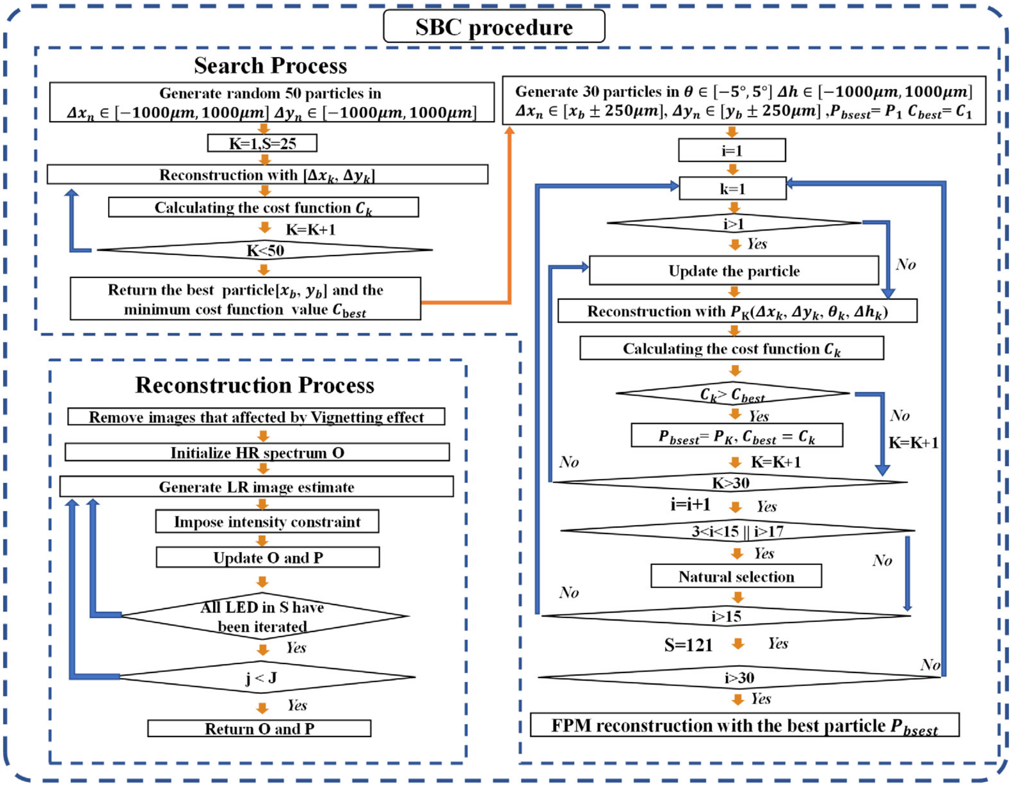

Fig. 3. The procedure of SBC.

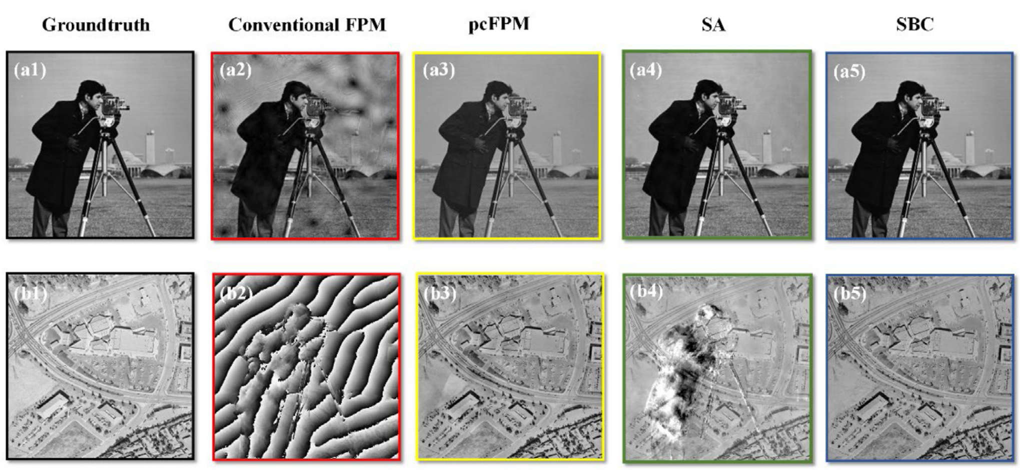

Fig. 4. Correction results of different algorithms. (a1)–(b1) High-resolution amplitude and phase images. (a2)–(b2) Reconstruction results of conventional FPM. (a3)–(b3) Reconstruction results of pcFPM. (a4)–(b4) Reconstruction results of SA algorithm. (a5)–(b5) Reconstruction results of the proposed method.

Table 3
Average corrected errors of different algorithm.

Algorithm	Δp	MSE
Convention FPM	4319	0.105
pcFPM	180	9.5×10^{-4}
SA	1802	0.0083
SBC	9.3	4.18×10^{-5}

4. Experiment

In order to evaluate the effectiveness of SBC through experiments, these methods are implemented in experimental data. A microscope with an Olympus objective (magnification 4×, NA = 0.1) is used to image the USAF target. A 15 × 15 LED array with the incident wavelength 620 nm is used to provide angle-varied illuminations. The distance between adjacent LED is 4 mm, and the distance between the sample and the LED array is 66 mm. A CCD camera (Lumenra, infinity-4) with pixel size of 9 μm is used for capturing the images. During the acquisition process, 225 low-resolution images are captured. The high-resolution target of USAF is located at the center FOV and the reconstruction results with different algorithms of it are shown in Fig. 6. The low-resolution image and its zoom-in are shown in Fig. 6(e1)–(e2). For conventional FPM, because it does not correct the position errors, the reconstruction quality of its amplitude is seriously degraded, as shown in Fig. 6 (a1)–(a2). For pcFPM, the results of Fig. 6 (b1)–(b2) are better than Fig. 6(a1)–(a2), but there are still some artifacts in it. Fig. 6 (c1)–(c2) show the corrected results of SA algorithm. Due to

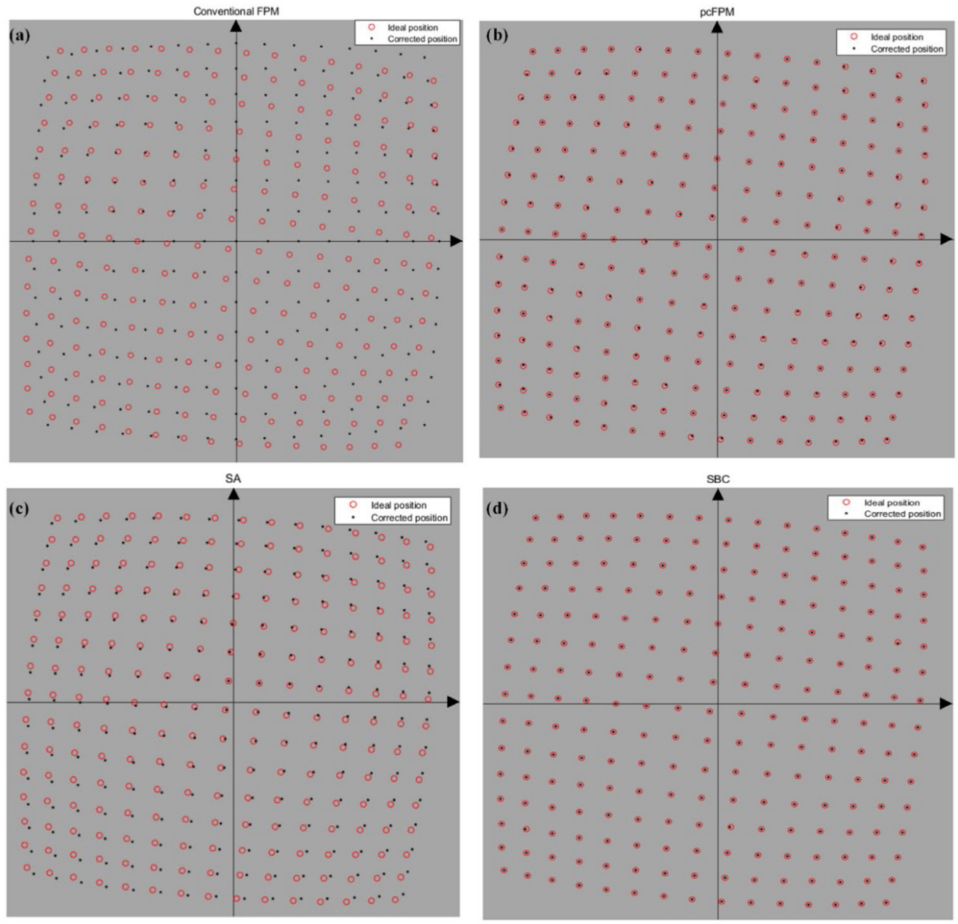

Fig. 5. The positions of frequency apertures corrected by different algorithms and the ideal frequency positions.

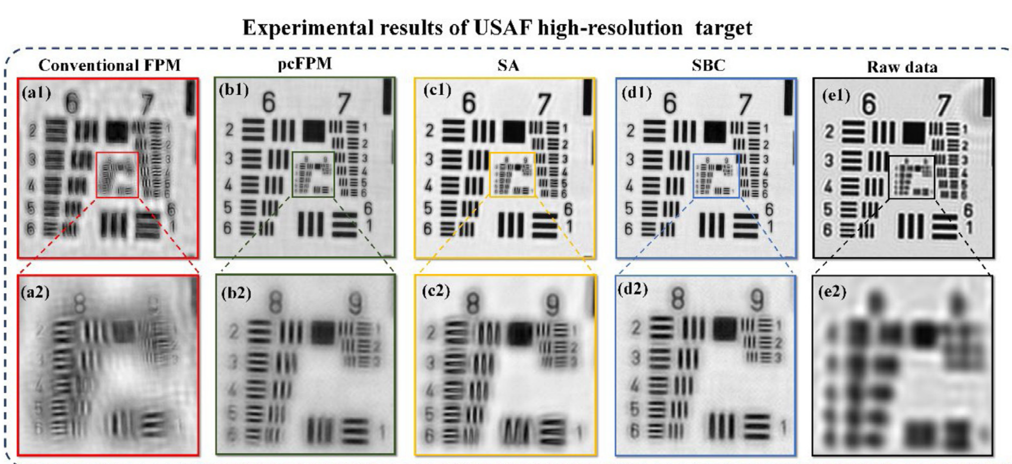

Fig. 6. Imaging experiments of USAF 1951. (a1)–(a2) Reconstruction results of conventional FPM. (b1)–(b2) Reconstruction results of pcFPM. (c1)–(c2) Reconstruction results of SA algorithm. (d1)–(d2) Reconstruction results of the SBC. (e1)–(e2) The captured low-resolution image of the USAF 1951 that located at the center FOV.

the limited search ability, the high-resolution target also falls into the local minimum value. For SBC, all the high-resolution target can be distinguished, as shown in Fig. 6(d1)–(d2). In the final reconstruction process, we use the background noise estimate method [19,40]. For the multiple system errors like noise, aberration and misalignment, a division-and-conquest strategy is more suitable [41].

Expected for the USAF target, we also employee the cervical smear for imaging experiment. The phase information can reveal the refractive index of the biological sample. It is more affected by misalignment error than amplitude. The reconstruction results of different algorithms are shown in Fig. 7. The captured low-resolution image is shown in Fig. 7 (e1). From Fig. 7 (a1)–(b1), because it is unable to deal with the misalignment errors, the reconstructed amplitude image and the phase image of conventional FPM converge into wrong value. From Fig. 7 (b1)–(b2), the pcFPM reconstructs the amplitude well, while artifacts exit in the phase image. For the reconstruction results of SA, shown in Fig. 7 (c1)–(c2), unexpected stripes appear in the amplitude and phase

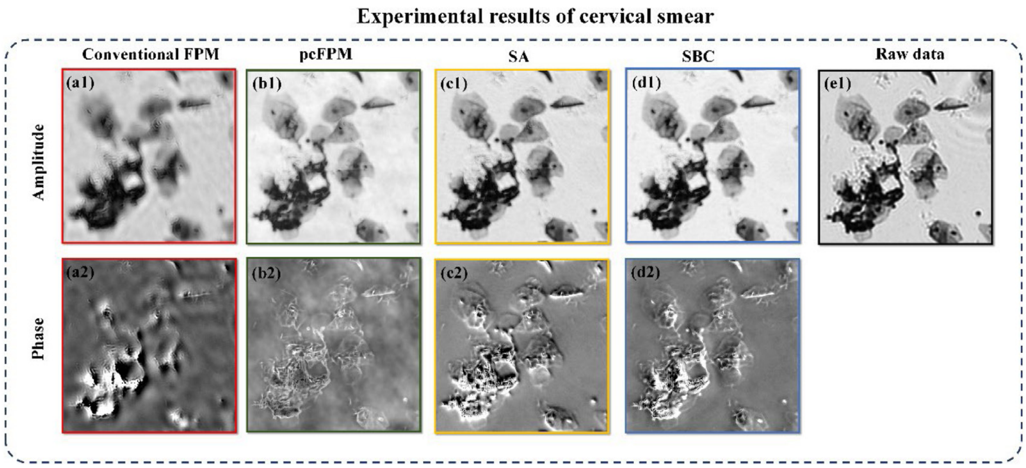

Fig. 7. Experimental results of cervical smear. (a1)–(d1) Reconstructed amplitude images of conventional FPM, pcFPM, SA, SBC respectively. (a2)–(d2) Reconstructed phase images of conventional FPM, pcFPM, SA, SBC respectively. (e1) The captured low-resolution image of cervical smear.

images. The proposed SBC method has better reconstructed amplitude and phase images without artifacts, shown in Fig. 7 (d1)–(d2).

5. Conclusion

In this paper, we proposed a misalignment error corrected method called SBC method. Different from the traditional misalignment error correction method, the SBC method uses the PSO algorithm to correct the four misalignment errors in space domain directly. In order to ensure the accuracy and efficiency of the searching process, natural selection and compressibility factor are introduced into the PSO algorithm. Compared with the traditional FPM and other advanced correction methods, the SBC method proposed in this paper has better reconstruction quality and higher accuracy. What we mean is to use this method to calibrate the system or calibrate the wavevector of each sub-field without reinstalling the system.

Declaration of competing interest

The authors declare that they have no known competing financial interests or personal relationships that could have appeared to influence the work reported in this paper.

Acknowledgment

This work is supported by CAS Interdisciplinary Innovation Team.

Funding

Department of Science and Technology of Jilin Province, China (20210101146JC, 20170519016JH), National Key R&D Program of China (2020YFA0714102), and National Natural Science Foundation of China (11604327, 11704377, 11804336, 61405194, 11774342, 61805238, 61475152, 61775212, 61811530061, 61378075 and 61377032).

References

[1] G. Zheng, R. Horstmeyer, C. Yang, Wide-field, high-resolution Fourier ptychographic microscopy, Nat. Photonics 7 (2013) 739–745.
[2] X. Ou, R. Horstmeyer, C. Yang, G. Zheng, Quantitative phase imaging via Fourier ptychographic microscopy, Opt. Lett. 38 (2013) 4845–4848.
[3] H. Faulkner, J.M. Rodenburg, Movable aperture lensless transmission microscopy: A novel phase retrieval algorithm, Phys. Rev. Lett. 93 (2004) 023903.
[4] A.M. Maiden, J.M. Rodenburg, M.J. Humphry, Optical ptychography: a practical implementation with useful resolution, Opt. Lett. 35 (2010) 2585–2587.
[5] M.J. Humphry, B. Kraus, A.C. Hurst, A.M. Maiden, J.M. Rodenburg, Ptychographic electron microscopy using high-angle dark-field scattering for sub-nanometre resolution imaging, Nature Commun. 3 (2012) 730.
[6] W. Luo, A. Greenbaum, Y. Zhang, A. Ozcan, Synthetic aperture-based on-chip microscopy, Light Sci. Appl. 4 (2015) e261.
[7] T.R. Hillman, T. Gutzler, S.A. Alexandrov, D.D. Sampson, High-resolution, wide-field object reconstruction with synthetic aperture Fourier holographic optical microscopy, Opt. Express 17 (2009) 7873–7892.
[8] T.M. Turpin, L.H. Gesell, J. Lapides, C.H. Price, Theory of the synthetic aperture microscope, Proc. SPIE - Int. Soc. Opt. Eng. 2566 (1995) 230–240.
[9] C. Polonschii, M. Gheorghiu, S. David, S. Gáspár, S. Melinte, H. Majeed, M.E. Kandel, G. Popescu, E. Gheorghiu, High-resolution impedance mapping using electrically activated quantitative phase imaging, Light Sci. Appl. 10 (2021) 20.
[10] M. Deng, S. Li, A. Goy, I. Kang, G. Barbastathis, Learning to synthesize: robust phase retrieval at low photon counts, Light Sci. Appl. 9 (2020) 36.
[11] F. Wang, Y. Bian, H. Wang, M. Lyu, G. Pedrini, W. Osten, G. Barbastathis, G. Situ, Phase imaging with an untrained neural network, Light Sci. Appl. 9 (2020) 77.
[12] K. Toda, M. Tamamitsu, T. Ideguchi, Adaptive dynamic range shift (ADRIFT) quantitative phase imaging, Light Sci. Appl. 10 (2021) 1.
[13] Q. Song, A. Baroni, R. Sawant, P. Ni, V. Brandli, S. Chenot, S. Vézian, B. Damilano, P. de Mierry, S. Khadir, P. Ferrand, P. Genevet, Ptychography retrieval of fully polarized holograms from geometric-phase metasurfaces, Nature Commun. 11 (2020) 2651.
[14] J. Sun, C. Zuo, L. Zhang, Q. Chen, Resolution-enhanced Fourier ptychographic microscopy based on high-numerical-aperture illuminations, Sci. Rep. 7, 1187.
[15] Z.F. Phillips, M.V. D'Ambrosio, L. Tian, J.J. Rulison, H.S. Patel, N. Sadras, A.V. Gande, N.A. Switz, D.A. Fletcher, L. Waller, Multi-contrast imaging and digital refocusing on a mobile microscope with a domed LED array, PLoS One 10 (2015) e0124938.
[16] Z.F. Phillips, R. Eckert, L. Waller, Quasi-dome: A self-calibrated high-NA LED illuminator for Fourier ptychography, in: Imaging Systems and Applications, 2017.
[17] A. Pan, Y. Zhang, K. Wen, M. Zhou, J. Min, M. Lei, B. Yao, Subwavelength resolution Fourier ptychography with hemispherical digital condensers, Opt. Express 26 (2018) 23119–23131.
[18] L. Tian, Z. Liu, L.H. Yeh, M. Chen, J. Zhong, L. Waller, Computational illumination for high-speed in vitro Fourier ptychographic microscopy, Optica 2 (2015) 904.
[19] L. Tian, X. Li, K. Ramchandran, L. Waller, Multiplexed coded illumination for Fourier ptychography with an LED array microscope, Biomed. Opt. Express 5 (2014) 2376–2389.
[20] Y. Zhou, J. Wu, Z. Bian, J. Suo, G. Zheng, Q. Dai, Fourier ptychographic microscopy using wavelength multiplexing, J. Biomed. Opt. 22 (2017) 66006.
[21] B. Lee, J. y. Hong, D. Yoo, J. Cho, Y. Jeong, S. Moon, B. Lee, Single-shot phase retrieval via Fourier ptychographic microscopy, Optica 5 (2018) 976–983.
[22] X. He, X. Pan, C. Liu, J. Zhu, Single-shot phase retrieval based on beam splitting, Appl. Opt. 57 (2018) 4832–4838.
[23] X. He, C. Liu, J. Zhu, Single-shot aperture-scanning Fourier ptychography, Opt. Express 26 (2018) 28187–28196.
[24] J. Sun, Q. Chen, J. Zhang, Y. Fan, C. Zuo, Single-shot quantitative phase microscopy based on color-multiplexed Fourier ptychography, Opt. Lett. 43 (2018) 3365–3368.

[25] X. Ou, G. Zheng, C. Yang, Embedded pupil function recovery for Fourier ptychographic microscopy, Opt. Express 22 (2014) 4960–4972.
[26] P. Song, S. Jiang, H. Zhang, X. Huang, Y. Zhang, G. Zheng, Full-field Fourier ptychography (FFP): Spatially varying pupil modeling and its application for rapid field-dependent aberration metrology, APL Photonics 4 (2019) 050802.
[27] T. Kamal, L. Yang, W.M. Lee, In situ retrieval and correction of aberrations in moldless lenses using Fourier ptychography, Opt. Express 26 (2018) 2708–2719.
[28] J. Chung, G.W. Martinez, K.C. Lencioni, S.R. Sadda, C. Yang, Computational aberration compensation by coded-aperture-based correction of aberration obtained from optical Fourier coding and blur estimation, Optica 6 (2019) 647–661.
[29] C. Zuo, J. Sun, Q. Chen, Adaptive step-size strategy for noise-robust Fourier ptychographic microscopy, Opt. Express 24 (2016) 20724–20744.
[30] Y. Zhang, P. Song, J. Zhang, Q. Dai, Fourier ptychographic microscopy with sparse representation, Sci. Rep. 7 (2017) 8664.
[31] L. Bian, J. Suo, G. Zheng, K. Guo, F. Chen, Q. Dai, Fourier ptychographic reconstruction using Wirtinger flow optimization, Opt. Express 23 (2015) 4856–4866.
[32] L. Bian, J. Suo, J. Chung, X. Ou, C. Yang, F. Chen, Q. Dai, Fourier ptychographic reconstruction using Poisson maximum likelihood and truncated Wirtinger gradient, Sci. Rep. 6 (2016) 27384.
[33] A. Pan, C. Zuo, Y. Xie, M. Lei, B. Yao, Vignetting effect in Fourier ptychographic microscopy, Opt. Lasers Eng. (2019).
[34] L.H. Yeh, J. Dong, J. Zhong, L. Tian, M. Chen, G. Tang, M. Soltanolkotabi, L. Waller, Experimental robustness of Fourier ptychography phase retrieval algorithms, Opt. Express 23 (2015) 33214–33240.
[35] R. Eckert, Z.F. Phillips, L. Waller, Efficient illumination angle self-calibration in Fourier ptychography, Appl. Opt. (2018).
[36] J. Sun, Q. Chen, Y. Zhang, C. Zuo, Efficient positional misalignment correction method for Fourier ptychographic microscopy, Biomed. Opt. Express 7 (2016) 1336.
[37] A. Zhou, W. Wang, N. Chen, E.Y. Lam, B. Lee, G. Situ, Fast and robust misalignment correction of Fourier ptychographic microscopy for full field of view reconstruction, Opt. Express 26 (2018) 23661–23674.
[38] H. Lee, B.H. Chon, H.K. Ahn, Rapid misalignment correction method in reflective fourier ptychographic microscopy for full field of view reconstruction, Opt. Lasers Eng. 138 (2021) 106418.
[39] J. Zhang, X. Tao, P. Sun, Z. Zheng, A positional misalignment correction method for Fourier ptychographic microscopy based on the quasi-Newton method with a global optimization module, Opt. Commun. 452 (2019) 296–305.
[40] M. Lei, A. Pan, Y. Zhang, Data preprocessing methods for robust Fourier ptychographic microscopy, Opt. Eng. 56 (2017) 1.
[41] A. Pan, Y. Zhang, T. Zhao, Z. Wang, D. Dan, B. Yao, System calibration method for Fourier ptychographic microscopy, J. Biomed. Opt. 22 (2017) 1.